Localization of protoporphyrin IX in glioma patients with paired stimulated Raman histology and two-photon excitation fluorescence microscopy

Mustafa Nasir-Moin
NYU Grossman School of Medicine https://orcid.org/0000-0002-0389-1852
Lisa Wadiura
Medical University Vienna https://orcid.org/0000-0002-9227-461X
Devin Juros
NYU Grossman School of Medicine https://orcid.org/0000-0003-1151-0738
Misha Movahed-Ezazi
NYU Grossman School of Medicine
Matthew Lee
NYU Grossman School of Medicine https://orcid.org/0000-0001-8816-1076
Hannah Weiss
NYU Grossman School of Medicine
Michael Müther
Münster University Hospital https://orcid.org/0000-0001-9427-5555
Daniel Alber
NYU Grossman School of Medicine
Sujay Ratna
Invenio Imaging https://orcid.org/0000-0002-0939-3715
Camila Fang
NYU Grossman School of Medicine https://orcid.org/0000-0002-8477-1253
Eric Suero-Molina
Münster University Hospital https://orcid.org/0000-0001-5652-2105
Sönke Hellwig
Münster University Hospital
Walter Stummer
University of Munster
Karl Rössler
Medical University Vienna
Johannes Hainfellner
Medical University Vienna
Georg Widhalm

Medical University Vienna
Barbara Kiesel
Medical University Vienna
David Reichert
Medical University Vienna
Mario Mischkulnig
Medical University Vienna
Rajan Jain
New York University https://orcid.org/0000-0002-4879-0457
Andrew Smith
NYU Grossman School of Medicine https://orcid.org/0000-0002-3990-2138
Jakob Straehle
Medical Center - University of Freiburg https://orcid.org/0000-0003-3063-8972
Nicolas Neidert
Medical Center - University of Freiburg https://orcid.org/0000-0003-0299-1138
Oliver Schnell
University of Freiburg
Jürgen Beck
Neurosurgery Freiburg
Jay Trautman
Invenio Imaging Inc.
Steve Pastore
Invenio Imaging
Donato Pacione
NYU Grossman School of Medicine
Dimitris Placantonakis
New York University Grossman School of Medicine
Eric Oermann
NYU Langone
John Golfinos
NYU Grossman School of Medicine
Todd Hollon
University of Michigan https://orcid.org/0000-0001-5987-6531
Matija Snuderl
New York University Medical Center
Christian Freudiger
Invenio Imaging Inc.
Dieter Henrik Heiland
Medical Center - University of Freiburg https://orcid.org/0000-0002-9258-3033

Daniel Orringer (Daniel.Orringer@nyulangone.org)
NYU Grossman School of Medicine https://orcid.org/0000-0001-6427-8376

Article

Keywords:

Posted Date: December 22nd, 2022

DOI: https://doi.org/10.21203/rs.3.rs-1519287/v1

Abstract

Fluorescence guidance is widely utilized to improve the precision of cancer surgery. 5-aminolevulinic acid, the most widely used fluorophore in glioma surgery, is thought to cause selective accumulation of fluorescent protoporphyrin IX (PpIX) in tumor cells. 5-aminolevulinic acid is highly specific for densely tumor-infiltrated tissue but less effective for visualizing the tumor periphery. To improve clinical detection of PpIX, we developed a microscope to perform paired stimulated Raman histology and two-photon excitation fluorescence microscopy (TPEF) and validated it in 175 fresh tumor specimens from 75 high-grade glioma patients across three institutions. Here, we demonstrate that intracellular PpIX accumulation occurs most prominently in histiocytic, rather than neoplastic, appearing cells. Spatially resolved metabolomics, transcriptomics and RNA sequencing revealed that PPIX is most avidly concentrated in tumor associated macrophages. There was no correlation between the degree of tissue cellularity and PpIX concentration across all imaged specimens (R=-0.21). Our findings encourage reconsideration of the existing theory of 5-ALA-induced glioma cell fluorescence and demonstrate how 5-ALA and TPEF imaging can provide a window into the immune microenvironment of human gliomas.

Introduction

The optimal surgical care of glioma patients requires a careful balance between maximal tumor resection and the preservation of neurologic function. Fluorescence guidance with 5-aminolevulinic acid (5-ALA) is one of the most well studied and evidence-supported approaches for maximizing extent of resection in high-grade glioma (HGG) patients.[1–3] The use of 5-ALA increases the chances for radiographically complete tumor resection, the clinical gold-standard in glioma surgery, by 63-89%.[1,3–7]

The best published evidence in glioblastoma (GBM) patients suggests that 5-ALA-induced fluorescence is most profound in densely tumor-infiltrated tissue and decreases towards the tumor periphery.[8,9] Unfortunately, widely employed techniques for visualization of 5-ALA-induced fluorescence are limited by poor sensitivity, particularly at tumor margins.[10] Consequently, the negative predictive value of 5-ALA-induced fluorescence in HGG has been estimated to be as low as 21%.[1,7,11–1]

Both cell-intrinsic factors such as altered heme metabolism and attributes of the brain tumor microenvironment are hypothesized to play a role in the 5-ALA induced fluorescence in high-grade gliomas. *In vitro* evidence suggests that 5-ALA causes fluorescence within glioma cells because of ferrochelatase dysfunction, which leads to intracellular accumulation of PpIX.[17–20] Several clinical studies point to a key role for blood brain barrier breakdown in determining which tumors will visibly fluoresce due to PpIX accumulation. Accordingly, fluorescence observed in glioma patients treated with 5-ALA is hypothesized to reflect both intracellular PPIX accumulation within tumor cells and local blood brain barrier breakdown.

Indeed, bright 5-ALA induced fluorescence is highly predictive for the presence of tumor infiltration[10]. Brain tissue infiltrated by a higher concentration of tumor cells- especially in regions where there is blood

brain barrier breakdown would, therefore, be hypothesized to fluoresce more strongly than brain tissue with a lesser degree of tumor infiltration behind an intact blood brain barrier. Low levels of 5-ALA induced fluorescence at glioma margins and in tumors with mild to moderate cellularity is thought to occur because of the challenge of detecting increasingly sparse fluorescing tumor cells where there is a low level of PpIX accumulation.[21]

Intriguingly, PpIX-induced tumor cell fluorescence in 5-ALA treated glioma tissue has not been well-documented.[22] Previously, we developed and validated an FDA-registered clinical stimulated Raman histology (SRH) microscopy system to streamline the process for accessing histologic data in the operating room.[23–26] SRH is achieved in the OR through the use of an Er-Yb fibre laser that can also be utilized to induce two-photon fluorescence. We hypothesized that creating a bifunctional imaging system capable of performing both SRH and two-photon fluorescence microscopy at precisely the same coordinates within tissue specimens would offer an unprecedented opportunity to directly visualize the microscopic localization of PpIX in human brain tumors. In addition the utilization of two-photon microscopic techniques enables optical sectioning in fresh human specimens, minimizing the decay of PpIX signal that can be caused by photobleaching and chemical degradation.

Our study in 75 high-grade glioma patients and three lymphoma patients yielded several unexpected findings. First, we noted that tissue cellularity did not correlate with 5-ALA-induced fluorescence. We also noted that PpIX accumulates most avidly in a subset of cells morphologically consistent with histiocytes in tumor infiltrated tissue. We verified the observation that PpIX accumulation occurred in tumor associated macrophages using spatially resolved metabolomics and RNA sequencing. Our data therefore create the possibility of a tumor cell-independent mechanism for PpIX accumulation in human brain tumors. This study also demonstrates how innovations in optics can advance our understanding of the cellular biodistribution of clinical fluorophores and offer a novel means of imaging the tumor-immune milieu.

Results

Engineering a multimodal optical system for SRH and TPEF

We modified an existing, FDA-registered clinical system for stimulated Raman histology (Fig. 1a-b) by adding a two-channel epi-fluorescence module to allow simultaneous detection of SRH and PpIX fluorescence from the same optical section in fresh human brain tumor specimens. Stimulated Raman scattering (SRS) is excited with a custom dual-wavelength picosecond (2-3ps) fibre laser source with a fixed wavelength pump beam at 790 nm and a Stokes beam tunable from 1010 nm to 1040 nm[27]. SRS is detected in transmission mode with a large area photo-diode (PD). As described previously[25], we combine high-frequency lock-in detection at 10MHz with high-speed auto-balanced detection in order to achieve high detection sensitivity. We use a high-NA water-immersion objective lens (Olympus 25x 1.05NA) to achieve high-resolution in tissue specimens. For SRH, we image the sample sequentially at 2845cm^{-1} to

detect primarily lipids and at 2940cm^{-1} to detect primary protein and DNA and apply a pseudo-color scheme that mimics traditional H&E staining.[25]

Two photon-fluorescence is generated by the same excitation beams used to achieve stimulated Raman scattering (Fig. 1a). We use a 700 nm long-pass dichroic (Edmund Optics 69-903) to direct the epi-fluorescence signal toward the dual-channel detector. The emission is filtered with a high optical-density 700 nm short-pass filter (Thorlabs FESH0700), split with a 50/50 beam splitter (Thorlabs BSW10R), filtered with a 640/75 nm (Edmund Optics 67-022) and 590/43 nm band-pass filter (Edmund Optics 67-020), and detected with two high-sensitivity photo-multiplier tube (PMT) detectors (Hamamatsu H10723-20), respectively. The two emission bands were chosen to match the 640 nm emission peak of PpIX and to be distinct but spectrally close in order to detect auto-fluorescence from species such as lipofuscin, NADH, and elastin (Fig 1C).

We detected the output from the PMT detector with two low-frequency analog-to-digital (ADC) detectors and display the 640 nm signal from PpIX and auto-fluorescent specimens in red and the 590 nm signal from primarily auto-fluorescent specimens in green (Fig. 1c). As a result, auto-fluorescence appears in hues of yellow and green depending on the specific emission ratio while signal in the red channel is primarily driven by the presence of PpIX. We display both the multiwavelength fluorescence and SRH images and display images from the same optical section side-by-side. The images are linked to enable zoom/pan functionality, allowing for a quick correlation of the images during surgery (Fig. 1b, Supplemental Videos 1-5).

Experimentally, we determined that the PpIX fluorescence was maximal when both the 790 nm and 1030 nm beams were present at the sample. However, this condition also creates coherent anti-Stokes Raman scattering (CARS) at 641 nm, which coincidentally falls into the 640 nm emission band and overwhelms the weaker PpIX signal. For this reason, we de-tune the time-delay between the 790nm and 1030nm beams, such that CARS is no-longer generated but two-photon excited fluorescence (TPEF) from 790 nm and 1030 nm is generated independently and measured with the 640 nm detector. We therefore modified the excitation sequence, in which we first image the sample with SRS at 2845cm-1, then with SRS at 2930 cm-1, and finally with TPEF, essentially scanning the same image strip three times. The order of this sequence is reversed during consecutive strips to minimize laser tuning and optimize imaging speed (i.e., the TPEF is detected first for every other strip). Striping is not visible in the stitched images, indicating that photo-bleaching does not present a major issue in this acquisition scheme.

Performance of paired SRH/TPEF microscope in standards and tissue

We validated the multimodal imaging system by measuring the fluorescence intensity of serial dilutions of soluble PpIX at known concentrations and found that 1.0 μg PpIX/ml was the threshold for detection (Supplementary Fig. 1). As expected, fluorescence intensity increased with increasing PpIX concentration between 1.0-62.5 μg/ml (Fig. 1d), a range that mirrors the concentration of PpIX clinically encountered in tumor-infiltrated tissue from glioma patients receiving 5-ALA.[28]

We then evaluated the ability of the SRH/TPEF microscope to visualize PpIX in brain tumor specimens from patients treated with 5-ALA prior to resection or biopsy of suspected high-grade glioma. We noted that the SRH/TPEF microscope produced SRH images acquired at the 2845 cm^{-1} and 2930 cm^{-1} Raman shifts of comparable character to previous SRH microscopes without the TPEF module, and that the TPEF images could be acquired in corresponding fields of view (Fig. 2). Based on morphologic evaluation, it was possible to visualize the same tissue architecture and cytology in the SRH and TPEF images.

Clinical detection of PpIX in brain tumor tissue typically occurs via microscopes that excite PpIX at approximately 405nm and detect emission at 600-710nm via a single photon excitation fluorescence (SPEF). To ensure the comparable image generation between the conventional SPEF microscopes commonly employed in the operating room and the laboratory and the TPEF-based system we engineered, we used both techniques to image comparable optical sections from the same specimens (Fig. 2J, Supplementary Figs. 2 and 3) and verified that the pattern of PpIX tissue distribution was comparable between SPEF and TPEF across a series of 30 specimens from 20 patients. We also measured the emission from 569-667nm with 405nm excitation of sectioned tumor specimens with SPEF and observed a spectral signature consistent with PpIX fluorescence with peak emission at 630nm (Supplementary Fig. 2). We also performed a photobleaching experiment with SPEF confocal microscopy to confirm that the areas of signal intensity and patterns attributed to PpIX fluorescence decayed with exposure to 405nm excitation while the areas with high signal intensity and patterns attributed to autofluorescence do not (Supplemental Fig. 4).

Measuring the correlation of tumor cellularity and fluorescence

Both neoplastic and non-neoplastic cells contain endogenous fluorophores[29]. To explore the possibility that the observed fluorescence in PMT1 was specific to 5-ALA administration, we imaged tissue from 5 high-grade glioma patients who had not received 5-ALA prior to resection. Importantly, in these cases the observed pattern of fluorescence revealed only structures that fluoresced in both channels (rather than solely in PMT1) suggesting that there was absence of PpIX present (Supplementary Fig. 5).

Having validated the performance of the SRH/TPEF imaging system in PpIX solutions and a small number of human specimens, we sought to systematically evaluate PpIX distribution in a cohort of high-grade glioma patients (n=70, Supplementary Table 1). The multimodal optical microscope we developed offered a unique opportunity to quantitatively study the relationship between tumor cellularity and fluorescence in high-grade gliomas. To make the best use of the complete microscopic imaging dataset we collected, we utilized QuPath's validated cell-detection module[30], to count all of the cells (n=2,504,733 cells, Fig. 3a) in all imaged specimens (n=163 and a total area of 3,175.5 mm^2) and developed a method for fluorescence quantification in the imaged specimens (Fig 3b). To quantify the fluorescence of PpIX, the signal from the PMT2 channel is regularized and subtracted from the PMT1 channel.

We noted a wide range of cellularity (average: 744 cells/mm^2, range: 285-1506 cells/mm^2) and fluorescence intensity amongst the specimens identified by operating surgeons as lesional and/or fluorescent during surgery (Supplementary Fig. 6). Using regression analysis of our entire dataset we also noted that there was no correlation between fluorescence and cellularity (R=-0.21, Fig. 3c, 3d).

Defining patterns of PpIX accumulation in high grade glioma tissue

Given the unexpected lack of correlation between cellularity and tissue fluorescence, we sought to better understand the nature of fluorescence in high-grade glioma tissue by characterizing the patterns of PpIX accumulation within tissue specimens. PpIX appeared to accumulate in both extracellular and intracellular spaces. Accumulation occurred to a variable degree both within individual specimens (Supplementary Fig. 7) and amongst patients (Fig. 4, Supplementary Fig. 6). Generally, there were three patterns of PpIX accumulation: (1) primarily autofluorescence (minimal PpIX accumulation, <5 a.u.), (2) dim PpIX fluorescence (5 - 40 a.u.) or (3) bright PpIX fluorescence (>40 a.u.). Intracellular concentration of PpIX occurred in two patterns, including: (1) axonal accumulation (935/166,743 or 0.6% fields of view, Supplementary Fig. 8) and (2) cytoplasmic accumulation (19,057/166,743 or 11.4% of fields of views, Supplementary Figs. 9 and 10). To better understand the variability in observed fluorescence, we examined a number of clinical variables with potential influence on the degree of observed fluorescence in study patients: the interval between 5-ALA dosing and specimen imaging (Supplementary Fig. 11), proportion of enhancing tumor, pattern of enhancement, and Ki-67 index.[31] Using a linear fixed effects model, none of these variables were found to correlate with the measured concentration of PpIX (Supplementary Table 2).

Identifying the cells concentrating PpIX in human brain tumors

Abundant evidence demonstrates intracellular accumulation of PpIX within glioma cell lines after treatment with 5-ALA in culture.[17–20] Notably, a definitive correlative study revealing PpIX within glioma cells in human tissues has not been reported. Intriguingly, an approach for PpIX visualization relying on light-sheet microscopy revealed accumulation of PpIX in a small minority of cells, many of which were in the perivascular space. The SRH/TPEF microscope we developed is particularly well suited for localization of PpIX in brain tumor tissue because it enables comparison of histomorphologic and fluorescent images of the same specimen in the same physical location with submicron resolution (Supplementary Videos 1-5).

Though rare in our dataset, we noted that 130,044/2,504,733 cells accumulated PpIX in the cytoplasm and that they generally exhibited morphology more consistent with histiocytes than tumor cells including reniform-shaped nuclei, a granular cytoplasmic appearance and variable cellular shape including both spherical and elongated forms (Supplementary Fig. 9). There was a high degree of variability in the abundance of cells with high intracellular PpIX concentration amongst and within subjects. However, cells with high intracellular PpIX concentrations were observed either along blood vessels (32/70 patients,

Supplementary Fig. 10) or infiltrating amongst tumor cells in 62/70 patients in a pattern consistent with the known distribution of histiocytes within high-grade gliomas[32].

Cytologic and histoarchitectural features led us to suspect cells concentrating PpIX intracellularly were myeloid cells, a subset of tumor cells or pericytes. We therefore employed immunostaining for markers of histiocytes (CD163+), tumor cells (GFAP+), and pericytes (SMA+) and in 5 cases (Supplementary Fig. 12).[33] In these cases, we noted that the abundance and morphology of cells with intracellular PpIX accumulation mirrored that of CD163+ cells in the imaged specimens. We then evaluated the abundance of CD163 in the 45 study subjects, in which imaged tissue was available for CD163+ immunohistochemistry by comparing the degree of CD163 positivity to the quantity of cells concentrating PpIX within their cytoplasm. The abundance of cells concentrating PpIX within their cytoplasm was closely associated with quantified CD163 positivity (Supplementary Fig. 12). The difference in the number of cells concentrating PpIX in the cytoplasm was greatest between tissues with the greatest CD163 positivity and those with the least CD163 positivity (p=0.002) but remained significant even when tissues with moderate CD163 positivity were compared to those with the least CD163 positivity (p=0.02 (Supplementary Fig. 12).

5-ALA-induced fluorescence in non-glial brain tumors has been previously reported.[34–38] Consequently, we hypothesized that PpIX might accumulate within CD163+ cells in non-glial tumors. In addition, there have been sporadic reports suggesting CD163 expression by glioma cells[39]. We examined tissue from three patients in whom 5-ALA was administered given a suspicion for high-grade glioma but were ultimately diagnosed with diffuse large B-cell primary central nervous system lymphoma. As observed in the glioma patients in the study, in tissue from CNS lymphoma biopsies, there was abundant intracellular accumulation of PpIX in cells that mirrored the population of CD163+ histiocytes, rather than in the neoplastic B-lymphocytes, in quantity and morphology (Supplementary Fig. 13).

Protoporphyrin IX is enriched in the myeloid cell population

To confirm the observation of elevated PpIX fluorescence intensity in macrophages, we leveraged recent integrated spatially resolved metabolomics (MALDI-FTICR-MSI) and transcriptomics (Visium 10X) data acquired from six GBM patients treated with 5-ALA[40] (Fig. 5a-b). PpIX is metabolized from 5-ALA via an intermediate compound, coproporphyrinogen III (CpPIII). We hypothesized that active PPIX metabolism is marked by the simultaneous expression of the heme biosynthesis enzymes *CPOX*, *HMBS* and *FECH* and the accumulation of intermediate metabolites (CpPIII and PpIX). Spatial correlation of the recently described regional transcriptional expression patterns (*Reactive Immune, Reactive Hypoxia, Spatial OPC, Radial Glia* and *Neuronal Development*[40]) with both 5-ALA intermediate metabolites (CpPIII, PpIX) and gene expression of *CPOX*, *HMBS* and *FECH* revealed high co-localization of 5-ALA metabolism with immune active regions (*Reactive Immune*) (Fig. 5c). The *Reactive Immune* regions are marked by a high content of mesenchymal-like malignant cells with CD163/HMOX1 immunosuppressive macrophages[41,42,43]. Heme oxygenase 1 (HMOX1) has been shown to be an important marker of increased Heme metabolism[44], which also suggests a key role of this subpopulation of macrophages in

PPIX metabolism. We noted that this observation was also consistent with the finding that myeloid cells, unlike CD45 negative cells, have a significantly enhanced PpIX fluorescence signal[45].

To verify the accumulation of PPIX in macrophages on a cellular level, we performed single cell deconvolution using the state-of-the-art Robust Cell Type Decomposition (RCTD)[46] and the GBMap reference dataset containing approximately ~1 million cells[47]. The inherent heterogeneity of PpIX accumulation in our specimens enabled us to compare cellular composition across areas of low and high PpIX accumulation (Fig. 5d). RCTD provided cell type likelihood scores for each spot which were spatially correlated to the expression of enzymes (in red) and metabolite intensities (in blue) (Fig. 5d and Supplementary Fig. 14a). Immunosuppressive tumor associated macrophages (TAM's) and inflammatory microglia demonstrated the strongest correlation with PpIX intensities and *HMBS* expression (Fig. 5d) with astrocyte-like malignant cells also showing a lesser degree of PpIX accumulation and *HMBS* and *FECH* expression. By extracting the mass spectra (regions of interest (ROI)) from both high CD163 expressing and non-expressing control regions we confirmed that higher PpIX intensity was present in macrophage-enriched regions (padj=0.0032) (Supplementary Fig. 14c-d).

To further validate our findings on an external, publicly available dataset, we utilized bulk RNA-seq obtained from PpIX positive cells separated with fluorescence-activated cell sorting (FACS) (Fig. 5e)[48]. Cell type deconvolution from bulk data by Multi-subject Single-cell Deconvolution (MuSiC)[49] and the GBMap dataset, demonstrated enrichment of myeloid and oligodendroglial lineages amongst PpIX positive cells. Focusing on the analysis of RNA-seq data from the tumor infiltration zone (Fig. 5f and Supplementary Fig. 14.d-e) is particularly valuable since it contains both malignant and non-malignant cells (Fig. 5f and Supplementary Fig. 14.d-e). Notably, malignant cells represented only 5% of the PpIX-positive cells isolated from infiltration zone tissue which was predominantly composed of tumor associated macrophages and oligodendroglial cells (Fig. 5f). The cellular composition of the PpIX-positive fraction was further investigated by inferred copy number alterations demonstrating the lack of the characteristic gain of chromosome 7 and loss of chromosome 10 in PpIX-positive cells (Supplementary Fig. 14f-g and Supplementary Fig. 15). In conclusion, IHC, spatially resolved metabolomics and transcriptomics, and PpIX enriched RNA-seq suggest that PPIX is synthesized and accumulates predominantly within myeloid cells.

Discussion

Improving the safety and accuracy of tumor resection is a long-standing focus in the field of surgical oncology. Given the challenge of delineating tumor from adjacent brain, intense effort has been dedicated towards developing technologies like 5-ALA fluorescence guidance- both with operating microscopes and handheld devices- to enable better visualization of tumor margins in glioma surgery.[21,50,51] Based on definitive improvements in completeness of resection in high-grade glioma surgery demonstrated by Stummer et al.[3] and the concept of metabolic targeting of abnormalities in the heme biosynthesis

pathway specific to glioma cells[52], 5-ALA has become a widely used adjunct in the field of neurosurgical oncology.

Regardless of the precise mechanism of accumulation of PpIX, a fluorescent metabolite of 5-ALA has been previously hypothesized to accumulate specifically in tumor cell cytoplasm, creating visible fluorescence. The evidence for glioma cell-specific accumulation is primarily based on *in vitro* studies and studies in animal models. While there are several studies that correlate observed fluorescence with the density of tumor cell infiltration in glioma specimens[1], there is a paucity of published evidence of 5-ALA-induced tumor fluorescence in human brain tumor specimens[21]. In addition, fluorescence has been reported in non-infiltrated tissue in glioma patients[10], perilesional tissue in metastatic tumor patients, inflammatory and dysplastic brain lesions.[53,54] Moreover, the accumulation of fluorescent protoporphyrins is well documented in non-glial tumors, both inside[55] and outside of the brain.[56,57]

To better understand the distribution of PpIX in brain tumors at the cellular level, we modified a bedside histologic imaging system that we previously developed for intraoperative use. This system enabled us to match virtual H&E and two-photon fluorescence images at the same location in the exact same optical tissue section, with submicron resolution in fresh unprocessed human brain tumor specimens. The impact of this unique optical system was unexpected as it demonstrated that PpIX accumulates both in the intracellular and extracellular spaces and that intracellular accumulation was most avid in tumor associated macrophages rather than tumor cells. These results are not consistent with the dogma that visible fluorescence in gliomas is driven by intracellular tumor cell accumulation of PpIX and should encourage a reconsideration of existing hypotheses on the mechanistic basis of observed PpIX accumulation within brain tumors.

5-ALA is reported to selectively accumulate within glioma cells due to their down-regulation of ferrochelatase but may also be impacted by dysregulation of ALA dehydrase, porphobilinogen deaminase, coproporphyrinogen oxidase, heme oxygenase, nitric oxide synthase as well as factors such as cell density and hypoxia[52]. While future work will be required to generate new theories of how PpIX accumulation occurs in brain tumors, existing evidence suggests accumulation of PpIX is most strongly influenced by the permeability of the blood brain barrier[58].

An important limitation of this study is that we focused on brightly fluorescing and/or lesional- appearing specimens taken predominantly within areas of pathologic, tumor-induced blood-brain barrier breakdown. It is likely that additional insight into the tissue distribution of PpIX in and around brain tumors will result from a systematic comparison of tissue sampled from uninvolved/minimally involved brain tissue (presumably with intact blood-brain barrier), the tumor periphery and viable core (where blood-brain barrier is dysfunctional). Another important limitation of this study is that the estimation of PpIX intensity in our specimens correlates with that seen in SPEF methods but may be impacted by the spectral properties of the TPEF microscope we engineered. Specifically, the microscope we developed is primarily designed to detect the physicochemical state of PpIX that emits at 634nm, rather than the state that emits at 620nm. However, the 620nm signal would show up in both PMTs. Notably, there was no

appreciable 620nm signal within tumor cells to suggest PpIX accumulation in a pattern distinct from the one appreciated with measured signal in PMT1.

That said, the evidence that PpIX accumulates in lesional-appearing and/or visually fluorescing tissue in a manner that is independent of tumor cell concentration combined with the finding that it accumulated in axons in 48.6% of patients in this study (34/70) has important clinical implications (Supplementary Fig. 8). Namely, surgeons should note that fluorescence may originate from tissue structures that are non-neoplastic and plausibly functional. The disconnection of tissue cellularity from visible fluorescence underscores the challenge of interpreting fluorescence during surgery and the importance of integrating anatomic, functional, imaging and gross visual cues in deciding to resect or preserve tissue encountered during surgery.

The discrepancy between the expected and observed location of PpIX on a cellular level speaks to the importance of assessing the expanding library of clinical fluorophores designed for use in fluorescence-guided surgery with optical systems that enable precise biodistribution studies. Through the use of an imaging system where tissues and individual cells can be microscopically assessed via both structural and fluorescence-based imaging modalities, it will be possible to verify fluorophore targeting rather than inferring it from low-resolution imaging methods or correlations between measured fluorescence and tissue cellularity.

The unexpected ability of the SRH/TPEF microscope to reveal intracellular PpIX accumulation within tumor associated macrophages is notable given the central role of the immune system in tumorigenesis[59], a current focus in the field of neuro-oncology on the development of antitumor immunomodulatory approaches[60,61] and the documented prognostic value of myeloid cells in GBM patients[62]. Histiocytes encompassing an array of myeloid immune cells including monocyte-derived macrophages and microglia and have the capacity to promote and interfere with glioma growth[63]. Recent evidence suggests a critical role for myeloid cells in glioblastoma patients who respond to anti-PD-1 immune checkpoint inhibitors[64]. Additional investigation is underway in our laboratory to better characterize the subset of immune cells that concentrate PpIX in high-grade glioma. Ultimately, PpIX may become a valuable microscopic imaging agent for assessing macrophage physiology in brain tumors at the time of diagnosis and, possibly, in the setting of immunotherapy.

Outlook

Combining stimulated Raman histology and two-photon fluorescence microscopy on a single optical platform offers a unique means of simultaneously visualizing tissue architecture and fluorophore distribution. Utilizing this system, we noted that PpIX accumulates in tissue specimens from 5-ALA-treated glioblastoma patients with variable distribution across the intracellular and extracellular tissue compartments. The finding that intracellular PpIX accumulation may occur within tumor-associated macrophages creates a new avenue for visualizing this critically important component of the tumor-immune microenvironment.

Methods

Study design

The inclusion criteria for this study were as follows: (1) adult males and females; (2) subjects undergoing brain-tumor resection at NYU Langone Medical Center, Medical University of Vienna, or Münster University Hospital (3) subjects (or designee) who provided informed consent or where a waiver of consent applied; (3) subjects who received 5-aminolevulinic acid two to twelve hours before tumor resection; (4) subjects with excess tumor tissue resected beyond that needed for diagnosis; and (5) subjects with a final diagnosis of a high-grade glioma.

The sample size was estimated at 70 patients to ensure adequate representation of all major tumor types for analysis and based on the design of previous studies comparing SRS and H&E. The central goals of this study were: (1) to build and verify a clinical microscope capable of performing both stimulated Raman spectroscopy and two-photon excited fluorescence microscopy; (2) to judge whether 5-aminolevulinic acid accumulated in tumor cells based on diagnostic histopathologic (SRH) images and TPEF images; and (3) to determine in which cells 5-aminolevulinic acid accumulated. We began by collecting biopsies ($N = 73$) from neurosurgical patients undergoing tumor resection. Each specimen was imaged immediately after removal with the SRS and TPEF microscope.

Tissue collection and imaging

Tissue was collected at NYU Langone Medical Center according to the NYU Langone IRB-approved protocol (IRB S19-01931), at the Medical University of Vienna according to the Medical University of Vienna-approved IRB protocol (419/2008 - Ethics Commission Medical University Vienna), and at the Münster University Hospital according to the Münster University-IRB protocol (2007-420-f-S and 2017-707-f-S). Tissue was imaged using the NIO Imaging System (Invenio Imaging, Inc) at a standard depth of 10 microns from the surface of the compressed tissue specimen and, after imaging, sent to the clinical pathology laboratory for downstream analysis afterwards. In a subset of cases with sufficient tissue beyond that needed for clinical diagnosis, tissue was immersed in saline or fixed in formalin for CD163 staining and/or single-photon microscopy. Single photon fluorescence images of specimens utilizing a standard confocal fluorescence microscope (Zeiss LSM 880) and TPEF images were obtained on tissues imaged with the NIO Laser Imaging system (Invenio Imaging Inc., Santa Clara).

Imaging Specimens with TPEF and SPEF

Tumor specimens to be imaged with the NIO Laser Imaging system were first split in half via surgical blade and divided into two portions: one portion to be imaged with paired SRH and TPEF microscopy and the other portion to be imaged with confocal SPEF microscopy. The confocal imaged portions were sealed without fixation on a standard glass microscope slide under a #1.5 thickness coverslip. All confocal images were collected immediately on an inverted Zeiss LSM 880 Laser Scanning Confocal Microscope with GaAsP detectors. Scans were performed with either a Plan-Apo 20x/0.8 M27 objective.

Fluorescence was excited using a 405 nm laser with a pinhole diameter of 1 Airy Unit and emission was acquired in Lambda scanning mode from 502-689nm with 9nm width increments. Both single fields and tile scans were collected; tile scans were stitched in Zen Black (Carl Zeiss).

TPEF Imaging PpIX serial dilutions

In order to provide reference for fluorescence that was detected on SRH images, we performed a dilution series of PpIX measured with TPEF. Pure PpIX was dissolved in 5% tween-20 Phosphate Buffered Saline (PBS) to create serial dilutions (0-125 microgram/ml), each with a 50% reduction in concentration of PpIX. The PpIX serial dilution solutions were imaged under 410nm excitation and imaged with the SRH/TPEF microscope. This serial dilution procedure was repeated three times and each dilution was measured three times for internal and external reproducibility. The fluorescence intensity was computed for each serial dilution and the average fluorescence intensity with 95% confidence intervals were calculated and plotted.

Fluorescence Quantification and Cell Counting

Each SRH and TPEF image pair was manually reviewed by D.J., and non-diagnostic regions of each image (e.g.,) were removed, which contain structures appearing like cells that can add noise to automated cell counting in the virtual H&E images and high autofluorescence that can add noise to the PpIX signal in the TPEF images. A sliding window algorithm was applied to generate 300 x 300-pixel patches from these cropped virtual H&E and TPEF images. All image patches were reviewed and autofluorescence, extracellular fluorescence, and intracellular fluorescence patterns were labeled by study authors (M.N., D.J., D.A., H.W., and M.M.).

To measure the fluorescence signal of endogenous fluorophores captured by the PMT1 and PMT2 filters, we computed the ratio of fluorescence in the PMT1 channel and the fluorescence in the PMT2 channel for each of the negative control cases. The mean PMT1 to PMT2 ratio for the negative control cases was used as a regularization term to remove the signal from endogenous fluorophores in the PpIX quantification.

$$\alpha = \frac{\sum_{\{negative\ controls\}} \frac{PMT1}{PMT2}}{|\{negative\ controls\}|}$$

The PpIX fluorescence was quantified for each TPEF patch by subtracting the averaged and regularized PMT2 channel from the average of the PMT1 channel.

Each patch from the virtual H&E images was analyzed using QuPath's watershed cell detection for Brightfield H&E images, which detected cells with a minimum area of 50 microns and a maximum area of 400 microns. The density of each patch was calculated as the number of cells in the patch divided by the

area of the patch in microns. The case level cell density was calculated as the total number of cells in the case divided by the total area of tissue imaged in the case.

$$caseCellDensity = \frac{\sum_{\{H\&E\ patches\}} |\{cells\}|}{\sum_{\{H\&E\ patches\}} area(patch)}$$

Each patch from the TPEF images was analyzed using QuPath's watershed cell detection for fluorescence images, which detected cells with a minimum area of 50 microns and a maximum area of 400 microns in the red channel. The density of each patch was calculated as the number of cells in the patch divided by the area of the patch in microns. The case level cell density was calculated as the total number of cells in the case divided by the total area of tissue imaged in the case.

A linear regression and its correlation coefficient were computed to map patients' average cellular density to their average fluorescence concentration.

CD163 Density Analysis

A representative section of formalin fixed paraffin-embedded (FFPE) tissue was subjected to immunohistochemical analysis using a clinically validated monoclonal antibody against CD163 (MRQ-26; Roche Diagnostics) to detect cells of monocyte/macrophage lineage within all cases that underwent ALA-imaging. Semi quantitative analysis of tumor-associated CD163 positive cells was categorized into three groups: low, medium and high. CD163 expression was quantified as the percentage of positive cells in a section as follows: Low - < 10% positive cells, Medium- ≥10-60% positive cells and High- >60% positive cells. Furthermore, CD163 immunoreactive cells were evaluated for focal or diffuse infiltration within the tumor tissue.

Radiologic Imaging Review

Preoperative MRI scans were evaluated by a radiology resident (M.L.) with the guidance of a board-certified neuroradiologist (R.J.). Lesions were classified by enhancement pattern (homogeneous, heterogeneous, necrotic ring, nodular, non-enhancing) as commonly described in clinical practice. Lesions were evaluated for enhancement quality, enhancing margin thickness, and enhancing margin definition according to the VASARI feature set (1), a validated system for describing glioma morphology on MRI. Segmentations of the enhancing tumor, non-enhancing tumor (including necrosis), and peritumoral edema on T1-weighted pre- and post-contrast, T2-weighted, and T2-FLAIR sequences were automatically generated using DeepMedic (2), a pre-trained brain tumor segmentation model, and manually corrected as needed (e.g., to include only the subsequently resected lesion). Segmentation volumes were calculated according to 1-mm isotropic voxels[65].

Differences between the fluorescing cell density between cases with varying CD163 density

CD163 density was assessed using a two-sided Mann-Whitney U Test. A linear fixed effects model was developed to assess the impact of the time between 5-ALA administration and imaging, the proportion of enhancing tumor, the pattern of the enhancement, and the Ki-67 proliferation index on the concentration of PpIX measured in each case. All analyses used a significance level of 0.05 and were conducted in R.

Spatial multi-omic Analysis

For spatial data analysis, we acquired the spatially resolved RNA-seq datasets using the SPATAData package (https://github.com/theMILOlab/SPATAData)[40]. The metabolomic (MALDI) data of 6 patients were downloaded (doi: https://doi.org/10.5061/dryad.h70rxwdmj). We aligned the metabolomic data to the transcriptomic profiles by affine transformation of the H&E images as described recently[40]. The metabolomic spectra were averaged across each transcriptomic spot with a size of 55µm. Annotations of metabolites were performed by the Metaspace (https://metaspace2020.eu) database using an FDR threshold of 10%. Spatially correlation analysis was performed by either a spatial Lag model or a Canonical Correlation Analysis (CCA). Cell type deconvolution of each spot was performed by Robust Cell Type Decomposition (RCTD) , a well validated toolbox[46]. The deconvolution was performed by the SPATAwrapper (https://github.com/heilandd-/SPATAwrappers) package using the function runRCTD. Visualization of surface plots or correlation analysis was performed by the SPATA2 toolbox.

Spatial Bulk and PpIX sorted RNA-seq Deconvolution and Analysis

For analysis of the spatial bulk and PpIX sorted cells, we used the recently published RNA-seq dataset[48]. The data contain samples from the tumor core area (Core), the contrast-enhancing rim (CE-Rim) and the infiltrative regions, which were defined as weak PpIX positive areas without defined histopathological classification which regions are samples according to the Ivy-GAP criteria. All samples (n=42) were deconvoluted to infer the cellular distribution using the pan-GBM single-cell data GBMap[47]. The full-scRNA-seq dataset was down-sampled by maintaining the quantitative distributions across all cellular subtypes, defined as “annotation level 4”. Cell type deconvolution was performed by the Multi-subject single cell deconvolution (MuSiC) algorithm[49] using the function music_prop. Copy number alterations (CNA) are performed by the SPATA2 toolbox using the runCnvAnalysis and the add-on functions from SPATAwrapper for visualization[46].

Copy Number Analysis

CNA analysis was performed using the CNA pipeline in the SPATA2 R tool available in the development branch, https://github.com/theMILOlab/SPATA2. Copy number variations (CNVs) were estimated by aligning genes to their chromosomal location and applying a moving average to the relative expression values, with a sliding window of 100 genes within each chromosome, as described recently.[66] First, genes were arranged in accordance to their respective genomic localization using the InferCNV package (R-software).[66] As a reference set of non-malignant cells, we used a spatial transcriptomic dataset from a non-malignant cortex sample. The exported .RDS output files were then reimported and rearranged to

defined chromosomal bins. These bins are created by the SPATAwrappers function Create.ref.bins(), with the SPATA object and the size of the given bins as input. A bin size of 1Mbp was used, resulting in 3847 chromosomal bins with a mean coverage of 5.5 genes per bin. Rescaling and interpolation was carried out using a 10kbp sliding window. For normalization, we used a loess regression model, built to determine the copy-number values from the InferCNV output. Interpolation and normalization were performed using the SPATAwrappers::runCNV.Normalization() function.[40]

Declarations

Reporting Summary

Further information on research design is available in the Nature Research Reporting Summary linked to this article.

Data availability

The data supporting the results in this study are available within the paper and its Supplementary Information. They can also be viewed at https://www.nio-net.com by logging-in with “PPIX” as the institution and with “Guest” as the user. All of the raw and processed-image data and patient data, including the representative images provided in the manuscript, are available from the authors on reasonable request, subject to approval from the Institutional Review Board of NYU Grossman School of Medicine.

Acknowledgements

Tanja Peilnsteiner, Alexandra Lang, NYU Langone’s Microscopy Laboratory (RRID: SCR_017934, and Yan Deng), NYU Langone Center for Biospecimen Research and Development (NIH/NCI 5P30CA016087-33), K12NS080223(TH) K12 grant, R01-CA226527 (DO)

Author contributions

M.N.M., L.I.W., M.S., and D.A.O. conceived of the study, designed the experiments, and wrote the article. D.J., M.M.E., M.L., E.S.M, W.S., R.J., D.Pl., E.K.O., J.H., B.K., D.R., M.M., and T.C.H. assisted in writing the article. M.N.M., L.I.W., D.J., M.M.E., M.L., S.H., H.W., M.M., D.A., S.R., S.P., C.F., A.S., J.S., N.N., O.S., J.B., and D.H.H. analyzed the data. M.N.M. and D.H.H. performed statistical analyses. C.W.F. and J.T. built the SRH/TPEF microscope. D.A.O., G.W., W.S., D.Pa., D.Pl., K.R. and J.G.G. provided surgical specimens for imaging.

Competing interests

D.A.O. and T.C.H. are medical advisors and shareholders of Invenio Imaging, Inc., a company developing SRH microscopes. M.M., W.S., and D.A.O. are consultants to NX Development Corporation, a company

that markets 5-ALA for clinical use. S.R, S.P, C.W.F. and J.K.T. are employees and shareholders of Invenio Imaging, Inc.

References

1. Stummer, W. et al. Fluorescence-guided resection of glioblastoma multiforme by using 5-aminolevulinic acid-induced porphyrins: a prospective study in 52 consecutive patients. J. Neurosurg. 93, 1003–1013 (2000).
2. Widhalm, G. et al. 5-Aminolevulinic acid is a promising marker for detection of anaplastic foci in diffusely infiltrating gliomas with nonsignificant contrast enhancement. Cancer 116, 1545–1552 (2010).
3. Stummer, W. et al. Fluorescence-guided surgery with 5-aminolevulinic acid for resection of malignant glioma: a randomised controlled multicentre phase III trial. Lancet Oncol. 7, 392–401 (2006).
4. Schucht, P. et al. 5-ALA complete resections go beyond MR contrast enhancement: shift corrected volumetric analysis of the extent of resection in surgery for glioblastoma. Acta Neurochir. 156, 305–12; discussion 312 (2014).
5. Della Puppa, A. et al. 5-aminolevulinic acid (5-ALA) fluorescence guided surgery of high-grade gliomas in eloquent areas assisted by functional mapping. Our experience and review of the literature. Acta Neurochir. 155, 965–72; discussion 972 (2013).
6. Schucht, P. et al. Gross total resection rates in contemporary glioblastoma surgery: results of an institutional protocol combining 5-aminolevulinic acid intraoperative fluorescence imaging and brain mapping. Neurosurgery 71, 927–35; discussion 935–6 (2012).
7. Díez Valle, R. et al. Surgery guided by 5-aminolevulinic fluorescence in glioblastoma: volumetric analysis of extent of resection in single-center experience. J. Neurooncol. 102, 105–113 (2011).
8. Stummer, W. et al. Predicting the ‘usefulness’ of 5-ALA-derived tumor fluorescence for fluorescence-guided resections in pediatric brain tumors: a European survey. Acta Neurochir. 156, 2315–2324 (2014).
9. Kiesel, B. et al. Systematic histopathological analysis of different 5-aminolevulinic acid-induced fluorescence levels in newly diagnosed glioblastomas. J. Neurosurg. 129, 341–353 (2018).
10. Lau, D. et al. A prospective Phase II clinical trial of 5-aminolevulinic acid to assess the correlation of intraoperative fluorescence intensity and degree of histologic cellularity during resection of high-grade gliomas. J. Neurosurg. 124, 1300–1309 (2016).
11. Panciani, P. P. et al. Fluorescence and image guided resection in high grade glioma. Clin. Neurol. Neurosurg. 114, 37–41 (2012).
12. Roberts, D. W. et al. Coregistered fluorescence-enhanced tumor resection of malignant glioma: relationships between δ-aminolevulinic acid-induced protoporphyrin IX fluorescence, magnetic resonance imaging enhancement, and neuropathological parameters. Clinical article. J. Neurosurg. 114, 595–603 (2011).

13. Coburger, J. et al. Tumor detection with 5-aminolevulinic acid fluorescence and Gd-DTPA-enhanced intraoperative MRI at the border of contrast-enhancing lesions: a prospective study based on histopathological assessment. Neurosurg. Focus 36, E3 (2014).
14. Yamada, S., Muragaki, Y., Maruyama, T., Komori, T. & Okada, Y. Role of neurochemical navigation with 5-aminolevulinic acid during intraoperative MRI-guided resection of intracranial malignant gliomas. Clin. Neurol. Neurosurg. 130, 134–139 (2015).
15. Panciani, P. P. et al. 5-aminolevulinic acid and neuronavigation in high-grade glioma surgery: results of a combined approach. Neurocirugia 23, 23–28 (2012).
16. Idoate, M. A., Díez Valle, R., Echeveste, J. & Tejada, S. Pathological characterization of the glioblastoma border as shown during surgery using 5-aminolevulinic acid-induced fluorescence. Neuropathology 31, 575–582 (2011).
17. Stummer, W. et al. In vitro and in vivo porphyrin accumulation by C6 glioma cells after exposure to 5-aminolevulinic acid. J. Photochem. Photobiol. B 45, 160–169 (1998).
18. Eléouet, S. et al. Heterogeneity of delta-aminolevulinic acid-induced protoporphyrin IX fluorescence in human glioma cells and leukemic lymphocytes. Neurol. Res. 22, 361–368 (2000).
19. Wu, S. M., Ren, Q. G., Zhou, M. O., Peng, Q. & Chen, J. Y. Protoporphyrin IX production and its photodynamic effects on glioma cells, neuroblastoma cells and normal cerebellar granule cells in vitro with 5-aminolevulinic acid and its hexylester. Cancer Lett. 200, 123–131 (2003).
20. Duffner, F. et al. Specific intensity imaging for glioblastoma and neural cell cultures with 5-aminolevulinic acid-derived protoporphyrin IX. J. Neurooncol. 71, 107–111 (2005).
21. **.** Valdés, Pablo A., et al. Quantitative fluorescence in intracranial tumor: implications for ALA-induced PpIX as an intraoperative biomarker. Journal of neurosurgery 115.1 (2011): 11-17.
22. Stummer, W. et al. Intraoperative detection of malignant gliomas by 5-aminolevulinic acid-induced porphyrin fluorescence. Neurosurgery 42, 518–25; discussion 525–6 (1998).
23. Hollon, T. C. et al. Near real-time intraoperative brain tumor diagnosis using stimulated Raman histology and deep neural networks. Nat. Med. 26, 52–58 (2020).
24. Hollon, T. C. et al. Rapid Intraoperative Diagnosis of Pediatric Brain Tumors Using Stimulated Raman Histology. Cancer Res. 78, 278–289 (2018).
25. Orringer, D. A. et al. Rapid intraoperative histology of unprocessed surgical specimens via fibre-laser-based stimulated Raman scattering microscopy. Nat Biomed Eng 1, (2017).
26. Hollon, T. C. et al. Rapid, label-free detection of diffuse glioma recurrence using intraoperative stimulated Raman histology and deep neural networks. Neuro. Oncol. 23, 144–155 (2021).
27. Freudiger, C. W. et al. Stimulated Raman Scattering Microscopy with a Robust Fibre Laser Source. Nat. Photonics 8, 153–159 (2014).
28. Suero Molina, E., Kaneko, S., Black, D. & Stummer, W. 5-Aminolevulinic Acid-Induced Porphyrin Contents in Various Brain Tumors: Implications Regarding Imaging Device Design and Their Validation. Neurosurgery 89, 1132–1140 (2021).

29. Leppert, J. et al. Multiphoton excitation of autofluorescence for microscopy of glioma tissue. Neurosurgery 58, 759–67; discussion 759–67 (2006).
30. Bankhead, P. et al. QuPath: Open source software for digital pathology image analysis. Sci. Rep. 7, 16878 (2017).
31. Capper, D. et al. DNA methylation-based classification of central nervous system tumours. Nature 555, 469–474 (2018).
32. Hambardzumyan, D., Gutmann, D. H. & Kettenmann, H. The role of microglia and macrophages in glioma maintenance and progression. Nat. Neurosci. 19, 20–27 (2016).
33. Louis, David N et al. The 2021 WHO Classification of Tumors of the Central Nervous System: a summary. Neuro-oncology vol. 23,8 (2021).
34. Kiesel, B. et al. 5-ALA-induced fluorescence as a marker for diagnostic tissue in stereotactic biopsies of intracranial lymphomas: experience in 41 patients. Neurosurg. Focus 44, E7 (2018).
35. Wadiura, L. I. et al. High Diagnostic Accuracy of Visible 5-ALA Fluorescence in Meningioma Surgery According to Histopathological Analysis of Tumor Bulk and Peritumoral Tissue. Lasers Surg. Med. 53, 300–308 (2021).
36. Millesi, M. et al. 5-ALA fluorescence for intraoperative visualization of spinal ependymal tumors and identification of unexpected residual tumor tissue: experience in 31 patients. J. Neurosurg. Spine 1–9 (2020).
37. Potapov, A. A. et al. Laser biospectroscopy and 5-ALA fluorescence navigation as a helpful tool in the meningioma resection. Neurosurg. Rev. 39, 437–447 (2016).
38. Marbacher, S. et al. Use of fluorescence to guide resection or biopsy of primary brain tumors and brain metastases. Neurosurg. Focus 36, E10 (2014).
39. Chen, T. et al. CD163, a novel therapeutic target, regulates the proliferation and stemness of glioma cells via casein kinase 2. Oncogene 38, 1183–1199 (2019).
40. Ravi, V. M. et al. Spatially resolved multi-omics deciphers bidirectional tumor-host interdependence in glioblastoma. Cancer Cell 40.6 (2022): 639-655.2.
41. Ravi, V. M. et al. T-cell dysfunction in the glioblastoma microenvironment is mediated by myeloid cells releasing interleukin-10. Nature communications 13.1 (2022): 1-16.
42. Mathewson, N. D. et al. Inhibitory CD161 receptor identified in glioma-infiltrating T cells by single-cell analysis. Cell 184.5 (2021): 1281-1298.
43. Hara, T. et al. Interactions between cancer cells and immune cells drive transitions to mesenchymal-like states in glioblastoma. Cancer Cell 39.6 (2021): 779-792.
44. Ito, H. et al. Oral administration of 5-aminolevulinic acid induces heme oxygenase-1 expression in peripheral blood mononuclear cells of healthy human subjects in combination with ferrous iron. European Journal of Pharmacology 833 (2018): 25-33
45. Pinton, L. et al. The immune suppressive microenvironment of human gliomas depends on the accumulation of bone marrow-derived macrophages in the center of the lesion. Journal for

immunotherapy of cancer 7.1 (2019): 1-14.

46. Cable, D. M. et al. Robust decomposition of cell type mixtures in spatial transcriptomics. Nature Biotechnology 40.4 (2022): 517-526.
47. Ruiz-Moreno, C. et al. Harmonized single-cell landscape, intercellular crosstalk and tumor architecture of glioblastoma. Preprint at https://www.biorxiv.org/content/10.1101/2022.08.27.505439v1.abstract (2022).
48. Smith, S. J. et al. Metabolism-based isolation of invasive glioblastoma cells with specific gene signatures and tumorigenic potential. Neuro-oncology advances 2.1 (2020): vdaa087.
49. Wang, X. et al. Bulk tissue cell type deconvolution with multi-subject single-cell expression reference. Nature communications 10.1 (2019): 1-9.
50. Valdés, Pablo A., et al. Quantitative fluorescence using 5-aminolevulinic acid-induced protoporphyrin IX biomarker as a surgical adjunct in low-grade glioma surgery. Journal of neurosurgery 123.3 (2015): 771-780.
51. Valdes, Pablo A., et al. 5-Aminolevulinic acid-induced protoporphyrin IX fluorescence in meningioma: qualitative and quantitative measurements in vivo. Operative Neurosurgery 10.1 (2014): 74-83.
52. Ma, R. & Watts, C. Selective 5-aminolevulinic acid-induced protoporphyrin IX fluorescence in Gliomas. Acta Neurochir. 158, 1935–1941 (2016).
53. Schatlo, Bawarjan, et al. 5-Aminolevulinic acid fluorescence indicates perilesional brain infiltration in brain metastases. World Neurosurgery: X 5 (2020): 100069.
54. La Rocca, Giuseppe, et al. 5-Aminolevulinic acid false positives in cerebral neuro-oncology: not all that is fluorescent is tumor. A case-based update and literature review. World Neurosurgery 137 (2020): 187-193.
55. Marhold, F. et al. Detailed analysis of 5-aminolevulinic acid induced fluorescence in different brain metastases at two specialized neurosurgical centers: experience in 157 cases. J. Neurosurg. 1–12 (2019).
56. Liu, Y. et al. Cytoreductive surgery under aminolevulinic acid-mediated photodynamic diagnosis plus hyperthermic intraperitoneal chemotherapy in patients with peritoneal carcinomatosis from ovarian cancer and primary peritoneal carcinoma: results of a phase I trial. Ann. Surg. Oncol. 21, 4256–4262 (2014).
57. Sari Motlagh, R. et al. Impact of enhanced optical techniques at time of transurethral resection of bladder tumour, with or without single immediate intravesical chemotherapy, on recurrence rate of non-muscle-invasive bladder cancer: a systematic review and network meta-analysis of randomized trials. BJU Int. 128, 280–289 (2021).
58. Müther, M., Jaber, M., Johnson, T. D., Orringer, D. A. & Stummer, W. A Data-Driven Approach to Predicting 5-Aminolevulinic Acid-Induced Fluorescence and World Health Organization Grade in Newly Diagnosed Diffuse Gliomas. Neurosurgery (2022) doi:10.1227/NEU.0000000000001914.
59. Brown, N. F., Carter, T. J., Ottaviani, D. & Mulholland, P. Harnessing the immune system in glioblastoma. Br. J. Cancer 119, 1171–1181 (2018).

60. Lim, M., Xia, Y., Bettegowda, C. & Weller, M. Current state of immunotherapy for glioblastoma. Nat. Rev. Clin. Oncol. 15, 422–442 (2018).
61. Ott, M., Prins, R. M. & Heimberger, A. B. The immune landscape of common CNS malignancies: implications for immunotherapy. Nat. Rev. Clin. Oncol. 18, 729–744 (2021).
62. Li, H. et al. Comprehensive Analysis of CD163 as a Prognostic Biomarker and Associated with Immune Infiltration in Glioblastoma Multiforme. Biomed Res. Int. 2021, 8357585 (2021).
63. Geribaldi-Doldán, N. et al. The Role of Microglia in Glioblastoma. Front. Oncol. 10, 603495 (2020).
64. Arrieta, V. A. et al. ERK1/2 phosphorylation predicts survival following anti-PD-1 immunotherapy in recurrent glioblastoma. Nat Cancer 2, 1372–1386 (2021).
65. Kamnitsas, K. et al. Efficient multi-scale 3D CNN with fully connected CRF for accurate brain lesion segmentation. Med. Image Anal. 36, 61–78 (2017).
66. Patel, Anoop P., et al. Single-cell RNA-seq highlights intratumoral heterogeneity in primary glioblastoma. Science 344.6190 (2014): 1396-1401.

Supplemental Videos

Supplemental Videos 1-5 are not available with this version.

Figures

Figure 1

Engineering a paired SRH/TPEF microscope: Building on an existing fiber laser-based microscope developed for clinical stimulated Raman scattering microscopy, we developed a paired SRH/TPEF microscope. 790 and 1010-1040nm excitation impulses are generated by a fiber laser and employed to induce both stimulated Raman scattering, collected in transmission via a photodiode and TPEF, collected in reflection, filtered as shown and detected with two high-sensitivity photo-multiplier tubes (**a**). SRH and TPEF images are displayed with the same fields of view in a split screen format (**b**). The ranges of emission detected by PMT1 (602-677 nm, red) PMT2 (570-620 nm, green) as well as their overlap (yellow) are shown on a graph depicting the emission spectra of PPIX, and autofluorophors NADH, flavins and lipofuscin (**c**). Fluorescence intensity increases in a dose dependent manner with increasing PpIX concentration (**d**).

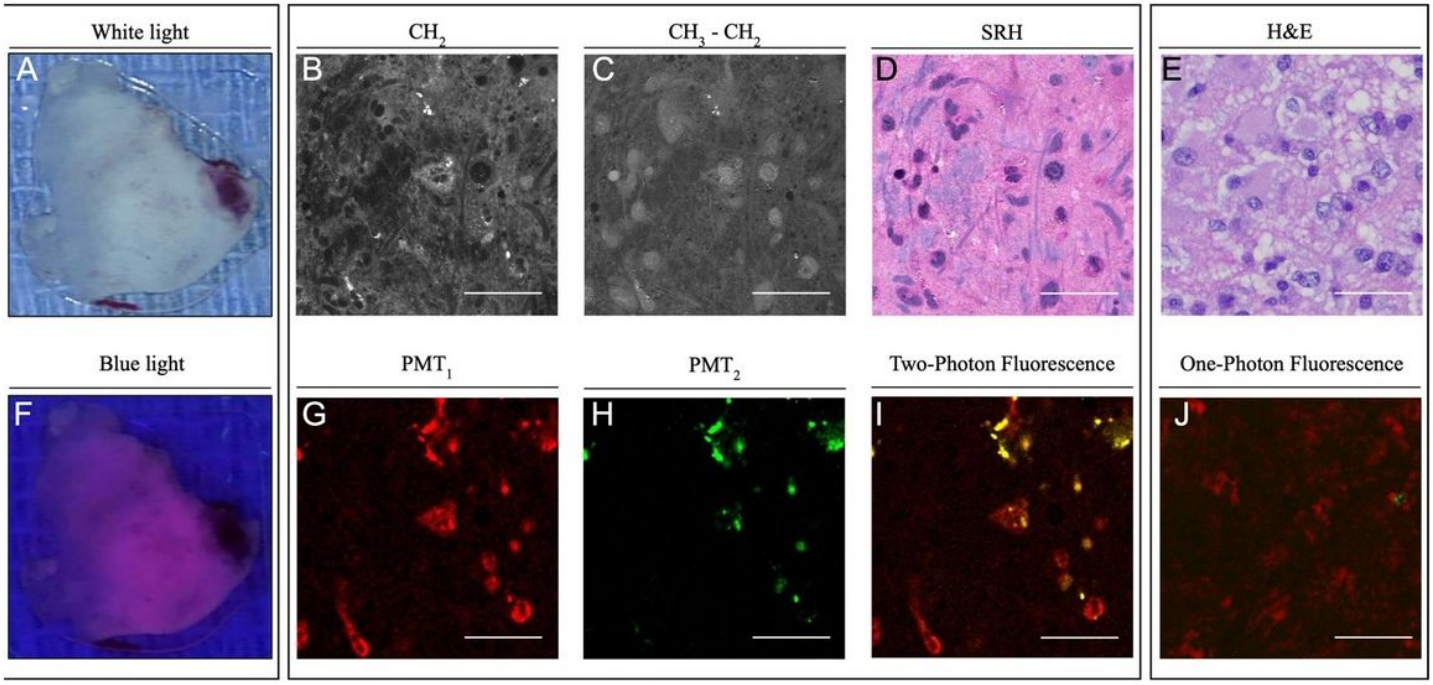

Figure 2

Paired SRH/TPEF Imaging. The engineered microscope enables imaging of fresh human brain tumor specimens (**a**). For each field of view, a 2845cm-1 stimulated Raman scattering image (revealing the distribution of CH2 bonds) (**b**) and a 2930cm-1 stimulated Raman scattering image (revealing the distribution of CH3 bonds) (**c**) are used to generate a stimulated Raman histologic image (**d**) that reveals architecture comparable to conventional H&E (**e**). To image the PpIX induced fluorescence in the same specimen that is visible with a Leica OH5 operating microscope (**f**), 640nm fluorescence (**g**) and 590 fluorescence images (**h**) are assigned to the red and green channels, respectively, to create a multichannel image that highlights the distribution of PPIX and autoflurophores (**i**). The two-photon excitation fluorescence image demonstrates a distribution of PpIX similar to that of a single photon excitation image collected in the same specimen (patient 43) (**j**).

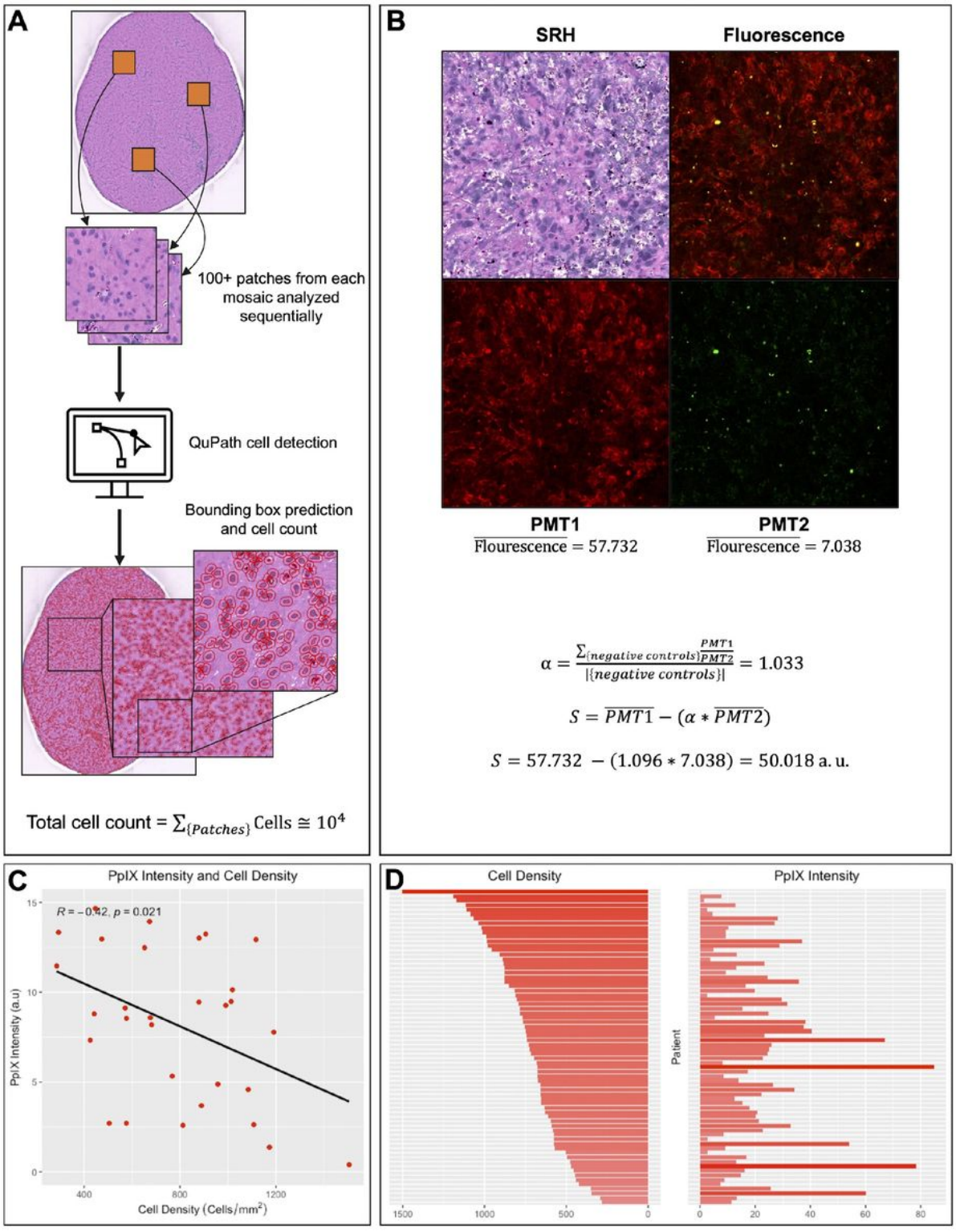

Figure 3

Relationship between cellularity and PpIX intensity (a.u.) in human gliomas. The QuPath cell detection module was employed to count each cell in each SRH mosaic (e.g., patient 9) (**a**). Another module was developed to quantify fluorescence in the PMT1 and PMT2 channels and to estimate the fluorescence signal attributable to PpIX (patient 48) (**b**). A linear regression analysis of measured cell density vs. PpIX intensity (a.u.) reveals no correlation (**c**). An alternative visualization of the relationship of cell density to

PpIX intensity (a.u.) with individual cases organized by decreasing cellularity to reveal the lack of correlation between the variables (**d**).

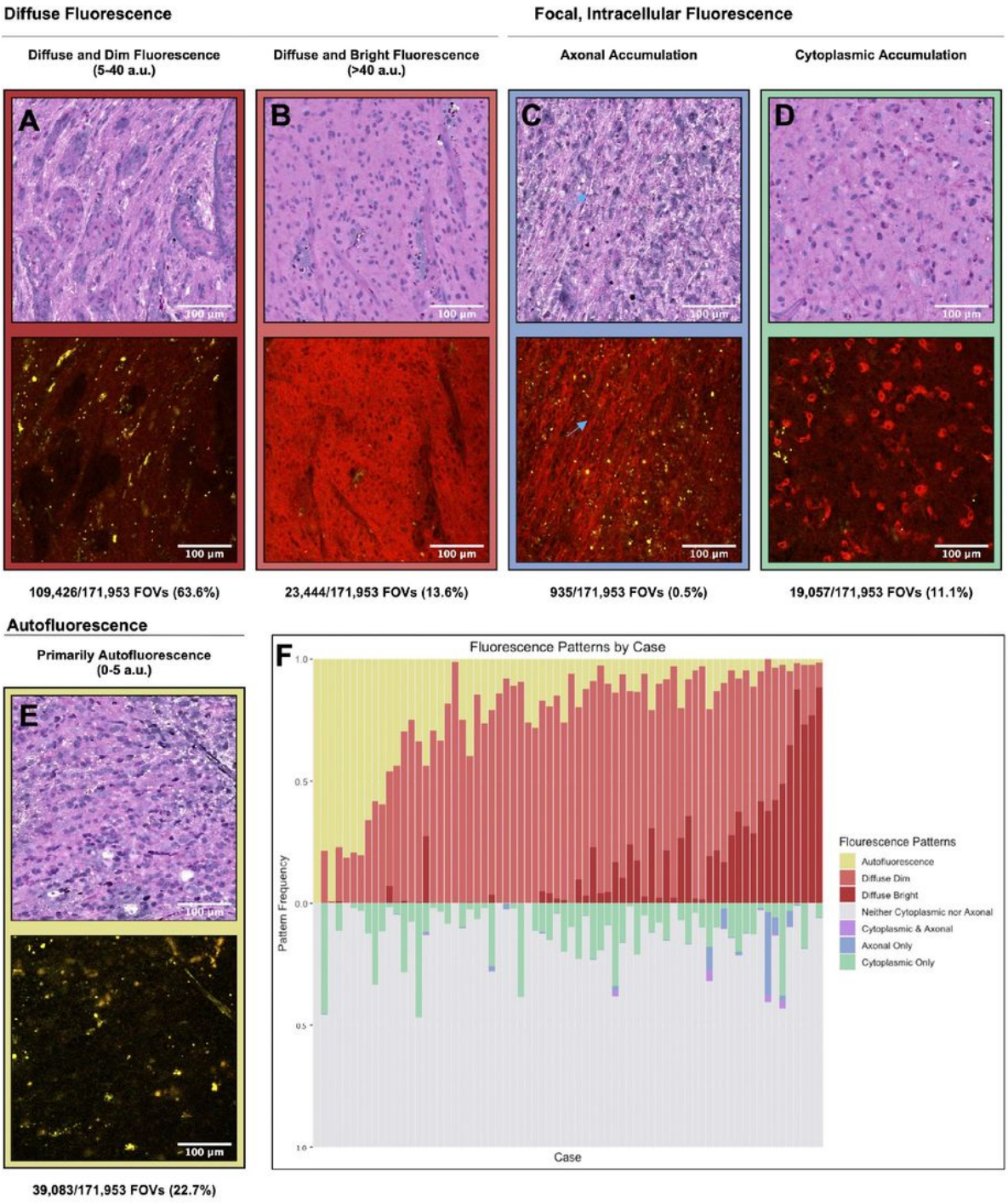

Figure 4

Patterns of PpIX distribution in human gliomas. Five predominant patterns of fluorescence were observed across the 163 specimens imaged in the study: primarily autofluorescence (**a**) diffuse and dim

fluorescence that is characterized by a low-level homogenous PMT-1 signal throughout the tumor except where vessels are present (patient 11), (**b**) diffuse and bright fluorescence where a higher PMT-1 signal is present in a homogenous pattern in the imaged tissue (patient 9), (**c**) axonal accumulation, where high PMT-1 signal is present most strongly in axons (patient 43), (**d**) cytoplasmic accumulation, where PMT-1 signal is focally present within a subset of imaged cells (patient 35), and (**e**) where fluorescent signal is present in both PMT channels resulting in a “yellow” speckled appearance (patient 13). The frequency of each pattern varies in each of the 70 cases (**f**), but diffuse and dim fluorescence was the most common pattern observed, accounting for 64.1% of the imaged fields of view.

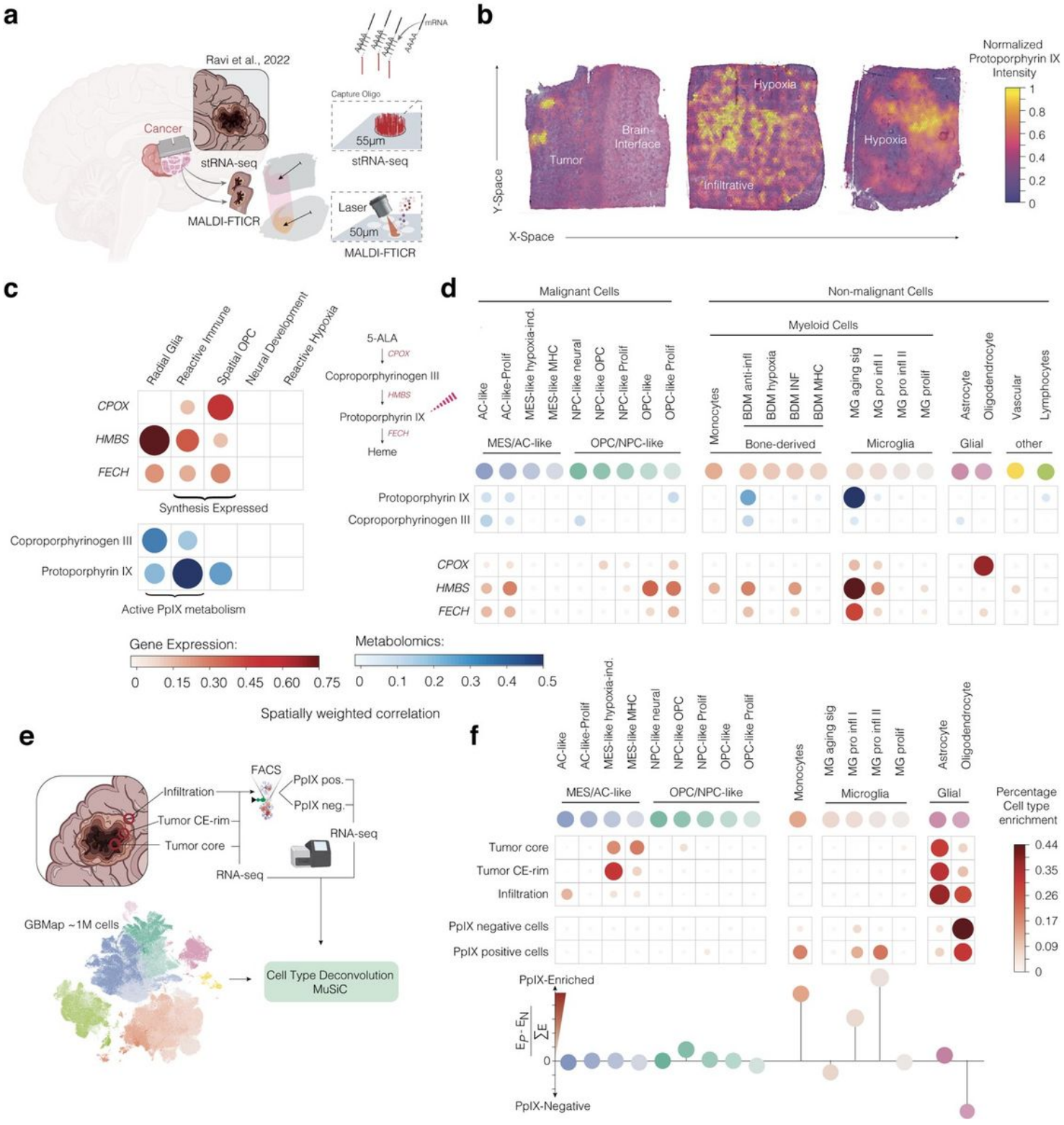

Figure 5

Transcriptomic and metabolomic analysis of PpIX accumulating cells. Illustration of the dataset and workflow (**a**). Examples of PpIX intensity in infiltrative areas and normal brain surface are indicated on the left, while examples of PpIX intensity in cellular tumor and hypoxia-associated areas of the tumor are shown on the right (**b**). The estimated spatial correlation of enzyme expression (red) and metabolites (blue) versus the enrichment of the spatial transcriptional programs in six patents is indicated in the dot

plot (**c**). The spatially weighted correlation analysis of enzymes (red) and metabolites (blue) with cell type likelihood scores in six patients is displayed in the dot plot (**c**). Illustration of the Smith et al, dataset[46] and integration with the GBMap single-cell dataset (**e**).The percentage of cell type enrichment of selected cell types are shown in (**f**). The differences of cell type enrichments between PpIX positive and negative samples are illustrated at the bottom in (**f**). *E,* represents the cell type enrichment score, y-axis demonstrate $E_{(PpIX+)} - E_{(PpIX-)}$ cells divided by the sum of cell type scores.

Supplementary Files

This is a list of supplementary files associated with this preprint. Click to download.

- SupplementalInformation.pdf